Mechanics of Materials 191 (2024) 104935

Contents lists available at ScienceDirect

Mechanics of Materials

journal homepage: www.elsevier.com/locate/mecmat

Research paper

On strength and toughness of soft staggered composites

Suhib Abu-Qbeitah *, Mahmood Jabareen, Konstantin Y. Volokh

Faculty of Civil and Environmental Engineering, Technion - Israel Institute of Technology, Haifa, Israel

ARTICLE INFO

To Alan Needleman, the Scientist and the Man

Keywords:
Fracture modeling
Bio-inspired composites
Nonlinear viscoelasticity
Material-sink approach

ABSTRACT

In the search of light yet strong and tough materials the nature produced soft composites with the staggered architecture. In such design, a soft protein matrix connects rigid mineral platelets similar to the cement connecting bricks in construction. In the present work, we examine strength and toughness (the total energy dissipated in fracture) of soft composites from the "first principles". The latter means that we do not postulate material strength and toughness in advance — they become an outcome of numerical solutions of the initial boundary value problem. We formulate the boundary value problem on the basis of the material-sink approach enforcing the damage description in constitutive equations. In addition to the classical nature-made staggered architecture, we examine some alternative possible designs of platelets inside the soft matrix. Comparisons show that the classical staggered design is the best one (among considered). Nature wins at the moment.

1. Introduction

Design of new materials is by no means trivial. However, we can learn from the nature who is a great designer. Natural materials can be mimicked by man. For instance, the nature is abundant in composite structures either at the micro or macro scales, such as biological fibers, gecko foot, mussel, and nacre. Such natural composites can be used as prototypes for the man-made bio-inspired materials that can replace metals, ceramics, and polymers in engineering and biomedical applications. For example, the bio-inspired collagen-reinforced hydroxyapatite can be used as the bone replacement material.

The ability of materials to resist failure and fracture are characterized by the material strength and toughness accordingly. The material strength is defined by the maximum stress that a typical specimen can tolerate under quasistatic loading. The strength is an indicator of material failure, which is the onset of damage. Quite often material strength is linked to material stiffness. That is generally wrong — these concepts are formally independent. Materials possessing both high stiffness and strength are often called hard materials and they are brittle.

Hard brittle materials can bear high loads before the onset of damage. Unfortunately, such materials and structures can break catastrophically after the onset of damage. Cracks are prone to fast propagation in brittle materials. In contrast, ductile materials resist the localized damage – cracks – by dissipating energy in inelastic deformations. The ability of materials to resist crack propagation via the energy dissipation is called toughness. Tough materials have high crack tolerance at the expense of the relatively low strength. Thus, material strength and toughness do not go hand in hand (Ritchie, 2011; Li et al., 2022; Kakisawa and Sumitomo, 2011).

Can we create materials with high strength and toughness simultaneously? The tentative answer is no, unfortunately. Fortunately, the nature created composite materials to compromise between strength and toughness. These composites are here for ages, created from limited materials and nontoxic processes (Huang et al., 2011). For example, Mollusk shells are composites. They demonstrate relatively high strength and toughness at the same time. They feature remarkable properties, which are unmatched by bio-inspired composites made by humans (Barthelat et al., 2009; Slesarenko et al., 2017b). Further, teeth of limpets employ a unique composite structure incorporating reinforcing fibers inside a soft protein. Due to that, the limpet's tooth demonstrates very high tensile strength up to 6.5 GPa (Barber et al., 2015), which indicates, probably, the strongest biological material (Slesarenko et al., 2017a) that beats the strength of the spider silk.

Most natural composites combine soft matrix with hard minerals to achieve the required load-bearing or armored shielding (Currey, 1999). It was shown in Wegst and Ashby (2004) that natural composites exhibit high stiffness by incorporating minerals in soft matrix that achieve remarkable toughness. In the human body, teeth and bones are good examples of mineralized tissues, where stiff minerals are bonded together by a soft matrix (Rabiei et al., 2010; Khayer Dastjerdi and Barthelat, 2015). Bone consists of HAP crystals – primarily composed of calcium and phosphorus – bonded together by the collagenous matrix (Libonati, 2016).

* Corresponding author.
E-mail address: a.suhib@campus.technion.ac.il (S. Abu-Qbeitah).

https://doi.org/10.1016/j.mechmat.2024.104935
Received 2 August 2023; Received in revised form 20 January 2024; Accepted 25 January 2024
Available online 1 February 2024

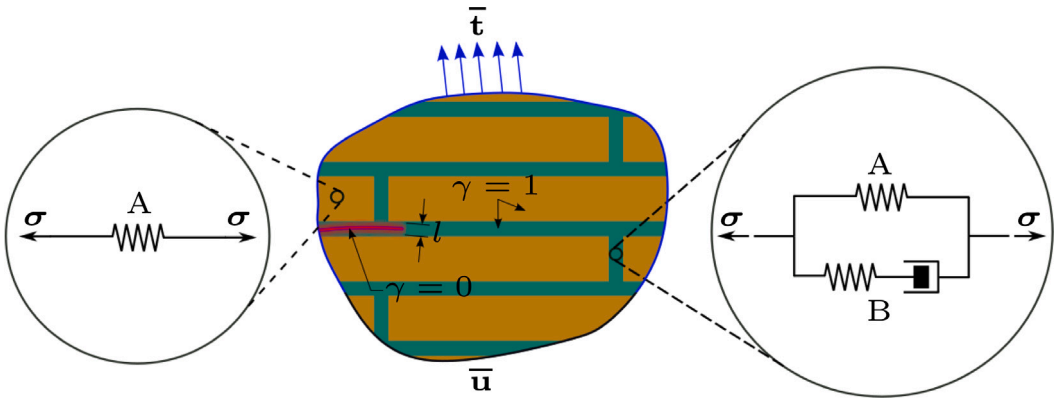

Fig. 1. Schematic representation of the material models for matrix (green) and inclusions (brown). (For interpretation of the references to color in this figure legend, the reader is referred to the web version of this article.)

Remarkably, the nature turns large amounts of hard brittle mineral pieces into tough bio-composites by binding them via a small amount of soft matrix. For example, organic soft material in Mollusk shells constitutes no more than 5 percent in weight, making these Mollusk shells about 1000 tougher than if they were composed only of minerals at the cost of a small decrease in stiffness (Barthelat et al., 2009). These mortar-and-brick microstructures appear to have the answer to our quest for the best materials.

Mechanical behavior of nacre has been studied by many researchers in various experiments, including uniaxial tension and simple shear tests (Currey and Sheppard, 1977; Menig et al., 2000; Barthelat et al., 2006, 2007; Barthelat and Espinosa, 2007; Peng et al., 2020). Nonetheless, it is not clear yet how these natural composites achieve a noticeable mechanical performance. Is it due to their architecture? Answering this question, Slesarenko et al. (2017b) concluded that the staggered architecture could not fully explain their remarkable strength and they hypothesized that new bonds might be created at the nano-scale. Though such hypothesis needs further examination, it should be mentioned that Slesarenko et al. (2017b) considered only the onset of material instability based on the energy limiters approach (Volokh, 2007, 2010, 2013, 2014) rather than simulated the full-scale damage and crack propagation. Thus, conclusions of Slesarenko et al. (2017b) are of limited impact.

Many studies were dedicated to design of composites mimicking mother nature (Tang et al., 2003; Dimas et al., 2013; Zhao et al., 2016; Gu et al., 2017; Slesarenko et al., 2017a; Milwich et al., 2006; Bhushan, 2009; Wegst et al., 2015; Bai et al., 2016; Luz and Mano, 2010; Studart, 2012; Libonati and Vergani, 2016; Barthelat and Rabiei, 2011; Libonati et al., 2014). It was realized that embedding soft materials (e.g., polymers) in ceramics in a wise design improves toughness manifestly (Wegst and Ashby, 2004). Also, bio-inspired composites created by embedding hard platelets in polymer matrix show high strength exceeding the one of many engineered polymers while preserving ductility (Bonderer et al., 2008). In other words, by changing the amount of the soft material and/or changing the geometrical configurations, it is viable to customize the mechanical efficiency of the desired composites (Cho et al., 2016; Dalaq et al., 2016). Such composite materials can be employed, for example, to control wave propagation (Rudykh and Boyce, 2014). It was shown in Magrini et al. (2019) that by adopting a bio-inspired structure, materials with antagonistic functional properties can be created. In Magrini et al. (2019), they fabricated bulk transparent materials with a nacre-like architecture yielding a tougher material – effectively arresting cracks – than ordinary glass, while keeping its optical transparency.

The present study aims at simulating failure and fracture of soft composites with the staggered design characterizing *de novo* bio-inspired materials. Various examples presented in this study are carried out with the goal of having guidelines for design of composites. In particular, the fracture patterns of nacre-inspired structures are revealed. Various geometric designs of the staggered composites are analyzed. They encompass different features such as inclined inclusions/matrix and waviness. Simulations answer various questions. For example, which structure – if any – effectively blocks the crack progress? Does the composite architecture affect toughness? Can we achieve a material with high toughness by adding a smaller fraction of soft matrix? Will the crack propagate in a specific region leading to a complete disintegration of the structure or no disintegration happens until most of the material is damaged?

The subsequent sections are arranged as follows. Section 2 summarizes the material-sink theory adopted in this work to model cracks. The discretization of the coupled problem is briefed in Section 3. Section 4 presents numerical examples to illustrate crack propagation in various composites structures. Conclusions are drawn in Section 5.

2. Material-sink theory

The material-sink (MS) theory is a relatively new method to model fracture (Volokh, 2017, 2019; Faye et al., 2019; Abu-Qbeitah et al., 2022, 2023b,a), which is based on the physical notion that broken bonds are diffused and mass is not preserved locally within the small damaged zone. The latter notion implies that mass density is an additional variable in the fracture problem. Below, the MS theory is briefly summarized.

2.1. Balance laws

The momentum and mass balance laws are defined as follows, respectively,

$$\varrho\dot{\mathbf{v}} = \mathrm{div}\boldsymbol{\sigma}, \quad \mathrm{div}\mathbf{s} + \xi = 0, \tag{1}$$

where ϱ is the mass density; $\mathbf{v}$ is the velocity vector; $\boldsymbol{\sigma}$ is the Cauchy stress tensor; $\mathbf{s}$ is the mass flux; ξ is the mass sink; and the divergence operator is defined with respect to the current coordinates.

The balance laws on the boundary provide the natural conditions $\boldsymbol{\sigma}\mathbf{n} = \bar{\mathbf{t}}$ and $\mathbf{s}\cdot\mathbf{n} = 0$, in which $\mathbf{n}$ is the unit outward normal and $\bar{\mathbf{t}}$ is the prescribed traction. Alternatively, the essential boundary condition $\mathbf{u} = \bar{\mathbf{u}}$ can be imposed on displacements.

2.2. Constitutive equations

The soft composite under consideration comprises relatively rigid platelets (bricks) embedded in much softer matrix providing the structural integrity of material – Fig. 1. For the soft matrix, we use the nonlinear viscoelasticity theory developed in Volokh (2019) and Abu-Qbeitah et al. (2023a). The rheological model of the so-called "standard

solid", shown in Fig. 1, underlays the tensorial formulation. In the latter formulation, the left Cauchy–Green tensor $\mathbf{b} = \mathbf{F}\mathbf{F}^{\mathrm{T}}$ describes deformation in spring A; the symmetric tensor $\mathbf{b}_B = \mathbf{b}_B^{\mathrm{T}}$ describes deformation in spring B; and the deformation rate tensor $\mathbf{d}_B = \mathbf{d}_B^{\mathrm{T}}$ describes flow in the dashpot. These tensors obey the following evolution equations

$$\dot{\mathbf{b}} = \mathbf{L}\mathbf{b} + \mathbf{b}\mathbf{L}^{\mathrm{T}}, \quad \dot{\mathbf{b}}_B = \left(\mathbf{L} - \mathbf{d}_B\right)\mathbf{b}_B + \mathbf{b}_B\left(\mathbf{L} - \mathbf{d}_B\right)^{\mathrm{T}}, \tag{2}$$

with the initial conditions: $\mathbf{b}(t = 0) = \mathbf{I}$ and $\mathbf{b}_B(t = 0) = \mathbf{I}$ and $\mathbf{d}_B(t = 0) = \mathbf{0}$ in which $\mathbf{L} = \mathrm{grad}\mathbf{v}$ is the velocity gradient tensor and $\mathbf{I}$ is the second-order identity tensor.

Cauchy stress $\boldsymbol{\sigma}$ is split in accordance with two branches of the rheological model

$$\boldsymbol{\sigma} = \boldsymbol{\sigma}_A + \boldsymbol{\sigma}_B, \tag{3}$$

where

$$\boldsymbol{\sigma}_A = 2\gamma\frac{\partial W_A}{\partial \mathbf{b}}\mathbf{b}, \quad \boldsymbol{\sigma}_B = 2\gamma\frac{\partial W_B}{\partial \mathbf{b}_B}\mathbf{b}_B, \tag{4}$$

Here $\gamma = \varrho/\varrho_0$ is the relative mass density having values between 0 and 1 corresponding to the fully damaged and intact states, respectively; ϱ and ϱ_0 are current and initial mass densities; W_A and W_B are the Helmholtz free energies per unit referential volume for springs A and B, respectively.

We specify the strain energies as follows

$$\begin{aligned} W_A &= \frac{1}{2}k^A_{\mathrm{bulk}}(J-1)^2 + c_1^A(\eta - 3) + c_2^A(\eta - 3)^2, \\ W_B &= \frac{1}{2}k^B_{\mathrm{bulk}}\left(J_B - 1\right)^2 + c_1^B\left(\eta_B - 3\right) + c_2^B\left(\eta_B - 3\right)^2, \end{aligned} \tag{5}$$

where $J = \det(\mathbf{F})$; $\eta = \mathrm{tr}\left(\mathbf{b}'\right)$; $\mathbf{b}' = J^{-2/3}\mathbf{b}$; $J_B = \sqrt{\det\left(\mathbf{b}_B\right)}$; $\eta_B = \mathrm{tr}\left(\mathbf{b}'_B\right)$; $\mathbf{b}'_B = J_B^{-2/3}\mathbf{b}_B$; and k^A_{bulk}, k^B_{bulk}, c_1^A, c_2^A, c_1^B, c_2^B are material constants.

The Cauchy stresses are determined by substituting (5) in (4) as follows

$$\begin{aligned} \boldsymbol{\sigma}_A &= \gamma k^A_{\mathrm{bulk}}(J-1)J\mathbf{I} + 2\gamma\left(c_1^A + 2c_2^A(\eta - 3)\right)\mathrm{dev}\mathbf{b}', \\ \boldsymbol{\sigma}_B &= \gamma k^B_{\mathrm{bulk}}\left(J_B - 1\right)J_B\mathbf{I} + 2\gamma\left(c_1^B + 2c_2^B\left(\eta_B - 3\right)\right)\mathrm{dev}\mathbf{b}'_B. \end{aligned} \tag{6}$$

Following Volokh (2019) and Abu-Qbeitah et al. (2023a), the Cauchy stress in the dashpot can be written as

$$\boldsymbol{\sigma}_B = \beta_1\mathbf{I} + \beta_2\mathbf{d}_B + \beta_3\mathbf{d}_B^2, \tag{7}$$

in which β_js are parameters, generally depending on deformation rates and stresses. It is reasonable to choose the following parameters (Volokh, 2019; Abu-Qbeitah et al., 2023a)

$$\beta_1 = \frac{1}{3}\mathrm{tr}\boldsymbol{\sigma}_B, \quad \beta_2 > 0, \quad \beta_3 = 0. \tag{8}$$

Using (8) and the reduced form of the dissipation inequality, the flow rule in the dashpot takes form

$$\mathbf{d}_B = \frac{1}{\beta_2}\mathrm{dev}\boldsymbol{\sigma}_B, \tag{9}$$

in which $\mathrm{dev}\boldsymbol{\sigma}_B = \boldsymbol{\sigma}_B - \frac{1}{3}(\mathrm{tr}\boldsymbol{\sigma}_B)\mathbf{I}$ is the deviatoric stress tensor.

The mass balance law can be rewritten in terms of the normalized mass flux $\mathbf{f}$ and the normalized mass sink ζ as follows

$$\mathrm{div}(\mathbf{f}) + \zeta = 0, \tag{10}$$

where the constitutive laws for $\mathbf{f}$ and ζ are as follows

$$\begin{aligned} \mathbf{f} &= l^2 I_3^{-1/2}\mathbf{b}\mathrm{grad}\left(I_3^{1/2}\gamma\right), \\ \zeta &= 1 - \frac{\gamma I_3^{1/2}}{\mathcal{H} + \varepsilon}, \end{aligned} \tag{11}$$

where l is the characteristic length and $I_3 = \det\mathbf{b}$.

The introduced history variable $\mathcal{H}$ guarantees the irreversibility of the damage, which is defined at computational time steps as follows

$$\mathcal{H}(t_0) = 1, \quad \mathcal{H}(t_{n+1}) = \min\left\{\begin{matrix} \exp\left[-\left(W_A/\Phi_A\right)^m\right] \\ \mathcal{H}(t_n) \end{matrix}\right\}, \tag{12}$$

where Φ_A is the energy limiter (or the average bond energy) per unit referential volume of spring A. Parameter m is a dimensionless material constant specifying the smoothness of the transition to material failure. The larger m the steeper is the transition to failure. Constant $\varepsilon = 10^{-15}$ is used to avoid singularity in computations.

We note that a description of the damage irreversibility can be included in the analytical model directly. However, such complication is unnecessary practically because the irreversibility can be readily enforced in a chosen computational algorithm.

Finally, we assume that the material model for inclusions is similar to the one of the matrix without the account of viscosity. Needless to say that the material constants of inclusions are different from the ones of the matrix. They are given below.

2.3. Integration of evolution equations

Eq. $(2)_1$ relating spring A strain rate $\dot{\mathbf{b}}$ and the velocity gradient $\mathbf{L}$; and Eq. $(2)_2$ relating spring B strain rate $\dot{\mathbf{b}}_B$ and the dashpot strain rate $\mathbf{d}_B$ and the velocity gradient $\mathbf{L}$, require algorithms to update all variables given at the start of the increment (at time t_n) to the time at the end of the increment (t_{n+1}).

First, we introduce the Oldroyd objective rate of the deformation tensor in spring B in the form

$$\overset{\diamond}{\mathbf{b}}_B \equiv \dot{\mathbf{b}}_B - \mathbf{L}\mathbf{b}_B - \mathbf{b}_B\mathbf{L}^{\mathrm{T}} = \mathbf{F}_r\partial(\mathbf{F}_r^{-1}\mathbf{b}_B\mathbf{F}_r^{-\mathrm{T}})/\partial t\mathbf{F}_r^{\mathrm{T}}, \tag{13}$$

where $\mathbf{F}_r = \partial\mathbf{x}/\partial\mathbf{x}^n$ is the relative deformation gradient and $\mathbf{x}$ and $\mathbf{x}^n$ are positions of a material point occupied at times t_{n+1} and t_n, respectively. Expressly, the relative deformation gradient implies the reference and current states at the beginning and the end of the time increment, respectively.

Substitution of (13) in $(2)_2$ with account of coaxiality (i.e., $\mathbf{d}_B\mathbf{b}_B = \mathbf{b}_B\mathbf{d}_B$) yields

$$\frac{\partial(\mathbf{F}_r^{-1}\mathbf{b}_B\mathbf{F}_r^{-\mathrm{T}})}{\partial t} = -2\mathbf{F}_r^{-1}\mathbf{d}_B\mathbf{b}_B\mathbf{F}_r^{-\mathrm{T}}, \tag{14}$$

with the initial condition $\mathbf{b}_B(t = 0) = \mathbf{I}$.

Using the explicit scheme of the time derivative on interval $[t_n, t_{n+1}]$, the temporal discretization of (14) is given by

$$\begin{aligned} (\mathbf{F}_r^{n+1})^{-1}\mathbf{b}_B^{n+1}(\mathbf{F}_r^{n+1})^{-\mathrm{T}} &= (\mathbf{F}_r^n)^{-1}\mathbf{b}_B^n(\mathbf{F}_r^n)^{-\mathrm{T}} \\ &\quad - 2\Delta t\,(\mathbf{F}_r^n)^{-1}\mathbf{d}_B^n\mathbf{b}_B^n(\mathbf{F}_r^n)^{-\mathrm{T}}, \end{aligned} \tag{15}$$

and $\Delta t = t_{n+1} - t_n$

$$\mathbf{F}_r^{n+1} = \mathbf{F}^{n+1}(\mathbf{F}^n)^{-1}, \quad \mathbf{F}_r^n = \mathbf{I}, \tag{16}$$

where superscripts n and $n + 1$ denote variables calculated at times t_n and t_{n+1}, respectively. Substitution of $(16)_2$ in (15) yields the explicit equation to determine the deformation tensor in spring B at time t_{n+1}

$$\mathbf{b}_B^{n+1} = \mathbf{F}_r^{n+1}\{\mathbf{I} - 2\Delta t\mathbf{d}_B^n\}\mathbf{b}_B^n(\mathbf{F}_r^{n+1})^{\mathrm{T}}. \tag{17}$$

Likewise, the deformation tensor in spring A (the left Cauchy–Green deformation tensor) at time t_{n+1} is determined as

$$\mathbf{b}^{n+1} = \mathbf{F}_r^{n+1}\mathbf{b}^n\left(\mathbf{F}_r^{n+1}\right)^{\mathrm{T}}. \tag{18}$$

2.4. Spatial tangent moduli

The implicit numerical algorithms utilized in the present study require analytical expressions for the spatial tangent moduli (Weickenmeier and Jabareen, 2014)

$$\mathbb{a} = \frac{1}{J}\frac{\partial\boldsymbol{\tau}}{\partial\mathbf{F}_r}\mathbf{F}_r^{\mathrm{T}} - \boldsymbol{\sigma}\oplus\mathbf{I}, \tag{19}$$

in which $\boldsymbol{\tau} = J\boldsymbol{\sigma}$ is the Kirchhoff stress, and the tensor product symbol $\oplus$ means: $(\mathbf{A}\oplus\mathbf{B})_{ijkl} = A_{il}B_{jk}$.

Specifically, the spatial tangent moduli corresponding to the adopted strain energies can be obtained by substituting (6) into (19) to yield

$$\begin{aligned}\mathbb{a} &= \gamma k^A_{\text{bulk}}\left(2J^2 - J\right)\mathbf{I}\otimes\mathbf{I} + 8\gamma c_2^A \text{dev}\mathbf{b}'\otimes\text{dev}\mathbf{b}' \\ &+ 2\gamma\left(c_1^A + 2c_2^A\left(\eta - 3\right)\right)\frac{\partial\,\text{dev}\mathbf{b}'}{\partial\mathbf{F}_r}\mathbf{F}_r^{\mathrm{T}} \\ &+ \gamma k^B_{\text{bulk}}\left(2J_B - 1\right)\mathbf{I}\otimes\frac{\partial J_B}{\partial\mathbf{F}_r}\mathbf{F}_r^{\mathrm{T}} + 4\gamma c_2^B \text{dev}\mathbf{b}'_B\otimes\frac{\partial\eta_B}{\partial\mathbf{F}_r}\mathbf{F}_r^{\mathrm{T}} \\ &+ 2\gamma\left(c_1^B + 2c_2^B\left(\eta_B - 3\right)\right)\frac{\partial\,\text{dev}\mathbf{b}'_B}{\partial\mathbf{F}_r}\mathbf{F}_r^{\mathrm{T}} - \boldsymbol{\sigma}\oplus\mathbf{I},\end{aligned} \tag{20}$$

where the explicit forms of the derivatives, $\left(\partial J_{\mathrm{B}}/\partial\mathbf{F}_r\right)\mathbf{F}_r^{\mathrm{T}}$, $\left(\partial\eta_{\mathrm{B}}/\partial\mathbf{F}_r\right)\mathbf{F}_r^{\mathrm{T}}$, $\left(\partial\text{dev}\mathbf{b}'/\partial\mathbf{F}_r\right)\mathbf{F}_r^{\mathrm{T}}$ and $\left(\partial\text{dev}\mathbf{b}'_{\mathrm{B}}/\partial\mathbf{F}_r\right)\mathbf{F}_r^{\mathrm{T}}$ are given in Abu-Qbeitah et al. (2023a).

3. Numerical formulation

Soft material of the matrix is usually almost incompressible. Such incompressibility feature is challenging for computations because it might lead to the so-called volumetric locking that distorts results of analysis. To suppress this undesirable numerical phenomenon, we adopt a mixed finite-element formulation that has been proposed by Weickenmeier and Jabareen (2014). Specifically, an infinitesimal material fiber at time t_n (i.e., $d\mathbf{x}^n$) is mapped to a material fiber at time t_{n+1} (i.e., $d\mathbf{x}$) via the following linear mapping

$$d\mathbf{x} = \mathbf{F}_r d\mathbf{x}^n, \quad \mathbf{F}_r = \mathbf{F}(\mathbf{F}^n)^{-1}, \quad \mathbf{F}_r^n = \mathbf{I}, \tag{21}$$

in which $\mathbf{F}$ and $\mathbf{F}^n$ are the deformation gradient tensors at times t_{n+1} and t_n, respectively, and $\mathbf{I}$ is the second-order identity tensor. Henceforward, any quantity with the superscript letter n means the quantity is calculated at time t_n, otherwise, the quantity is calculated at time t_{n+1}.

In this study, the coupling between momentum balance law $(1)_1$ and mass balance law $(1)_2$ is carried out using the staggered scheme. On the one hand, the momentum balance is solved for the displacement degrees of freedom (DOFs) based on the relative density DOF from the previous iteration. On the other hand, the mass balance is solved for the mass density DOF based on the displacement DOFs calculated from the previous iteration.

In the following subsections, the mixed finite-element formulation is briefly outlined. For more details about the finite-element formulation, interested readers are advised to consult (Weickenmeier and Jabareen, 2014; Abu-Qbeitah et al., 2023a). According to Weickenmeier and Jabareen (2014) and Abu-Qbeitah et al. (2023a), the deformation gradient, the relative deformation gradient, and the deformation gradient at time t_n are modified as follows

$$\widetilde{\mathbf{F}} = \widetilde{\mathbf{F}}_r\widetilde{\mathbf{F}}^n, \quad \widetilde{\mathbf{F}}_r = \left(\frac{\overline{J}_r}{J_r}\right)^{1/3}\mathbf{F}_r, \quad \widetilde{\mathbf{F}}^n = \left(\frac{\overline{J}^n}{J^n}\right)^{1/3}\mathbf{F}^n, \tag{22}$$

where $\overline{J}_r$, as will be explained in the next subsection, is the ratio of the element's domain at time t_{n+1} to the element's domain at time t_n; J_r is the determinant of the relative deformation gradient; $\overline{J}^n$ is the ratio of the element's domain at time t_n to the referential element's domain; and J^n is the determinant of the deformation gradient at time t_n.

3.1. Discretization of the momentum balance law

The weak form of the momentum balance is given by $\delta\Pi^u = \sum_{e=1}^{N_{el}}\delta\Pi_e^u = 0$, where N_{el} is the number of elements in the domain. The variation of the potential energy of the momentum balance can be written using the Hu–Washizu principle with respect to the independent fields including the modified relative deformation gradient $\widetilde{\mathbf{F}}_r$, the assumed dilatation measure $\overline{J}_r$, and the assumed hydrostatic pressure $\overline{p}$. The weak form of the momentum balance of a typical finite element (Weickenmeier and Jabareen, 2014) can be written as

$$\begin{aligned}\delta\Pi_e^u &= \int_{\Omega_e}\rho\ddot{\mathbf{u}}\cdot\delta\mathbf{u}\,d\Omega_e + \int_{\Omega_e}\widetilde{\widetilde{\boldsymbol{\sigma}}}:\delta\mathbf{h}\,d\Omega_e - \delta\Pi_e^{u,\text{ext}} \\ &+ \int_{\Omega_e^n}\left(J_r - \overline{J}_r\right)\delta\overline{p}\,d\Omega_e^n + \int_{\Omega_e^n}\left(\frac{\overline{J}^n}{J^n}\widetilde{p} - \overline{p}\right)\delta\overline{J}_r\,d\Omega_e^n,\end{aligned} \tag{23}$$

where the subscript e means the element level; $\ddot{\mathbf{u}}$ is the acceleration vector; $\delta\mathbf{u}$ is the virtual displacement vector; Ω_e is the element domain at time t_{n+1}; Ω_e^n is the element domain at time t_n; $\overline{p}$ is a scalar related to the hydrostatic pressure; and $\delta\Pi_e^{u,\text{ext}}$ is the virtual work of external forces. Further, the quantities $\{\widetilde{\widetilde{\boldsymbol{\sigma}}}, \delta\mathbf{h}, \widetilde{p}\}$ are given by

$$\widetilde{\widetilde{\boldsymbol{\sigma}}} = \frac{\overline{J}}{J}\text{dev}\left(\widetilde{\boldsymbol{\sigma}}\right) + \overline{p}\mathbf{I}, \quad \delta\mathbf{h} = \frac{\partial\delta\mathbf{u}}{\partial\mathbf{x}}, \quad \widetilde{p} = \frac{1}{3}\widetilde{\boldsymbol{\sigma}}:\mathbf{I}. \tag{24}$$

Here, $J = \det(\mathbf{F})$ and $\overline{J}$ (dilatation measure) are defined at time t_{n+1} to the referential element's domain and $\widetilde{\boldsymbol{\sigma}}$ is the sum of the modified stresses in branches A and B calculated using the modified deformation tensors.

The modified deformation tensors in branches A and B are determined based on the modified relative deformation gradient as follows

$$\begin{aligned}\widetilde{\mathbf{b}} &= \widetilde{\mathbf{F}}_r\widetilde{\mathbf{b}}^n\left(\widetilde{\mathbf{F}}_r\right)^{\mathrm{T}}, \\ \widetilde{\mathbf{b}}_B &= \widetilde{\mathbf{F}}_r\{\mathbf{I} - 2\Delta t\widetilde{\mathbf{d}}_B^n\}\widetilde{\mathbf{b}}_B^n(\widetilde{\mathbf{F}}_r)^{\mathrm{T}},\end{aligned} \tag{25}$$

in which $\widetilde{\mathbf{d}}_B^n$ is the modified deformation rate tensor in the dashpot at the beginning of the time increment, calculated based on the modified Cauchy stress in branch B.

Variations of fields $\overline{J}_r$ and $\overline{p}$ vanish due to the assumption they are constant at the element level. Thus, the last two terms in (23) are zeros leading to the following expressions

$$\overline{J}_r = \frac{1}{\Omega_e^n}\int_{\Omega_e^n}J_r\,d\Omega_e^n, \quad \overline{p} = \frac{1}{\Omega_e^n}\int_{\Omega_e^n}\frac{\overline{J}^n}{J^n}\widetilde{p}\,d\Omega_e^n. \tag{26}$$

For deriving the stiffness matrix, the weak form of the linear momentum balance is linearized with respect to the displacement field as follows

$$\begin{aligned}\Delta\delta\Pi_e^u &= \int_{\Omega_e}\rho\Delta\ddot{\mathbf{u}}\cdot\delta\mathbf{u}\,d\Omega_e \\ &+ \int_{\Omega_e}\left\{\delta\mathbf{h}:\left(\widetilde{\mathbb{a}}_{uu}:\Delta\mathbf{h} + \widetilde{\mathbf{a}}_{u\overline{J}_r}\frac{\Delta\overline{J}_r}{\overline{J}_r} + \mathbf{I}\Delta\overline{p}\right)\right. \\ &+ \frac{\delta\overline{J}_r}{\overline{J}_r}\left(\widetilde{\mathbf{a}}_{\overline{J}_r u}:\Delta\mathbf{h} + \widetilde{a}_{\overline{J}_r\overline{J}_r}\frac{\Delta\overline{J}_r}{\overline{J}_r} - \frac{\overline{J}_r}{J_r}\Delta\overline{p}\right) \\ &+ \left.\delta\overline{p}\left(\mathbf{I}:\Delta\mathbf{h} - \frac{\overline{J}_r}{J_r}\frac{\Delta\overline{J}_r}{\overline{J}_r}\right)\right\}d\Omega_e,\end{aligned} \tag{27}$$

where

$$\begin{aligned}\widetilde{\mathbb{a}}_{uu} &= \left(\mathbb{I} - \frac{1}{3}\mathbf{I}\otimes\mathbf{I}\right):\frac{\overline{J}}{J}\widetilde{\mathbb{a}}:\left(\mathbb{I} - \frac{1}{3}\mathbf{I}\otimes\mathbf{I}\right) \\ &- \frac{1}{3}\left(\text{dev}\left(\widetilde{\widetilde{\boldsymbol{\sigma}}}\right)\otimes\mathbf{I} + \mathbf{I}\otimes\text{dev}\left(\widetilde{\widetilde{\boldsymbol{\sigma}}}\right)\right) \\ &+ \left(\frac{\overline{J}}{J}\widetilde{p} - \overline{p}\right)\mathbf{I}\oplus\mathbf{I} + \left(\overline{p} - \frac{1}{3}\frac{\overline{J}}{J}\widetilde{p}\right)\mathbf{I}\otimes\mathbf{I}, \\ \widetilde{\mathbf{a}}_{u\overline{J}_r} &= \frac{1}{3}\left(\mathbb{I} - \frac{1}{3}\mathbf{I}\otimes\mathbf{I}\right):\frac{\overline{J}}{J}\widetilde{\mathbb{a}}:\mathbf{I} + \frac{1}{3}\text{dev}\left(\widetilde{\widetilde{\boldsymbol{\sigma}}}\right), \\ \widetilde{\mathbf{a}}_{\overline{J}_r u} &= \frac{1}{3}\mathbf{I}:\frac{\overline{J}}{J}\widetilde{\mathbb{a}}:\left(\mathbb{I} - \frac{1}{3}\mathbf{I}\otimes\mathbf{I}\right) + \frac{1}{3}\text{dev}\left(\widetilde{\widetilde{\boldsymbol{\sigma}}}\right), \\ \widetilde{a}_{\overline{J}_r\overline{J}_r} &= \frac{1}{9}\mathbf{I}:\frac{\overline{J}}{J}\widetilde{\mathbb{a}}:\mathbf{I} - \frac{2}{3}\frac{\overline{J}}{J}\widetilde{p}.\end{aligned} \tag{28}$$

Here $\mathbb{I}_{ijkl} = \delta_{ik}\delta_{jl}$ is the fourth order identity tensor and $\widetilde{\mathbb{a}}$ is the modified spatial tangent moduli determined from (19), calculated using the modified relative deformation gradient ($\widetilde{\mathbf{F}}_r$), the modified left Cauchy–Green deformation tensor ($\widetilde{\mathbf{b}}$), and the modified deformation tensor in spring B ($\widetilde{\mathbf{b}}_B$).

Displacements and virtual displacements are approximated as follows

$$\underline{\mathbf{u}} = \sum_{I=1}^{n_{en}} N_I \underline{\hat{\mathbf{u}}}^I = \underline{\underline{\mathbf{N}}}_u \underline{\hat{\mathbf{u}}}, \quad \delta\underline{\mathbf{u}} = \sum_{I=1}^{n_{en}} N_I \delta\underline{\hat{\mathbf{u}}}^I = \underline{\underline{\mathbf{N}}}_u \delta\underline{\hat{\mathbf{u}}}, \tag{29}$$

where Voigt notation has been employed. According to this notation, first and second-order tensors are represented by columns with a single underline while fourth-order tensors are represented by matrices with a double underline. Also n_{en} is the number of nodes per element and N_I is the shape function for node I.

For the brick element, for example, $\underline{\hat{\mathbf{u}}}$ and $\delta\underline{\hat{\mathbf{u}}}$ contain all nodal displacements and all nodal virtual displacements as follows

$$\underline{\hat{\mathbf{u}}} = \left\{\underline{\hat{\mathbf{u}}}^1, \underline{\hat{\mathbf{u}}}^2, \ldots, \underline{\hat{\mathbf{u}}}^8\right\}^{\mathrm{T}}, \quad \delta\underline{\hat{\mathbf{u}}} = \left\{\delta\underline{\hat{\mathbf{u}}}^1, \delta\underline{\hat{\mathbf{u}}}^2, \ldots, \delta\underline{\hat{\mathbf{u}}}^8\right\}^{\mathrm{T}}, \tag{30}$$

and $\underline{\underline{\mathbf{N}}}_u$ is a matrix incorporates shape functions as defined in Abu-Qbeitah et al. (2023a).

Then, the gradient of virtual displacements takes form

$$\delta\underline{\mathbf{h}} = \sum_{I=1}^{8} \underline{\underline{\mathbf{B}}}_I \delta\underline{\hat{\mathbf{u}}}^I = \underline{\underline{\mathbf{B}}}_u \delta\underline{\hat{\mathbf{u}}}, \quad \underline{\underline{\mathbf{B}}}_u = \left[\underline{\underline{\mathbf{B}}}_1 \quad \underline{\underline{\mathbf{B}}}_2 \quad \cdots \quad \underline{\underline{\mathbf{B}}}_8\right], \tag{31}$$

where $\delta\underline{\mathbf{h}}$ is the matrix form of the tensor $\delta\mathbf{h}$ as follows: $\delta\underline{\mathbf{h}} = \left\{\delta h_{11}, \delta h_{22}, \delta h_{33}, \delta h_{12}, \delta h_{21}, \delta h_{23}, \delta h_{32}, \delta h_{31}, \delta h_{13}\right\}^{\mathrm{T}}$, and the matrix $\underline{\underline{\mathbf{B}}}_u$ is a 9×24 matrix, which contains all $\underline{\underline{\mathbf{B}}}_I$, $I = 1, \ldots, 8$, where each $\underline{\underline{\mathbf{B}}}_I$ is 9×3 matrix including the derivatives of the nodes' shape functions with respect to the current coordinates.

Now, the nodal external, internal, and inertia forces take the following forms, respectively,

$$\begin{aligned} \underline{\hat{\mathbf{F}}}_e^{u,\mathrm{ext}} &= \int_{\partial\Omega_e} \underline{\underline{\mathbf{N}}}_u^{\mathrm{T}} \underline{\bar{\mathbf{t}}}\, d\Gamma_e, \quad \underline{\hat{\mathbf{F}}}_e^{u,\mathrm{int}} = \int_{\Omega_e} \underline{\underline{\mathbf{B}}}_u^{\mathrm{T}} \underline{\tilde{\boldsymbol{\sigma}}}\, d\Omega_e, \\ \underline{\hat{\mathbf{F}}}_e^{u,\mathrm{iner}} &= \int_{\Omega_e} \rho_0 \gamma \underline{\underline{\mathbf{N}}}_u^{\mathrm{T}} \underline{\ddot{\mathbf{u}}}\, d\Omega_e, \end{aligned} \tag{32}$$

where $\underline{\tilde{\boldsymbol{\sigma}}} = \left\{\tilde{\sigma}_{11}, \tilde{\sigma}_{22}, \tilde{\sigma}_{33}, \tilde{\sigma}_{12}, \tilde{\sigma}_{21}, \tilde{\sigma}_{23}, \tilde{\sigma}_{32}, \tilde{\sigma}_{31}, \tilde{\sigma}_{13}\right\}^{\mathrm{T}}$.

After the discretization, (27) reads

$$\Delta\delta\Pi_e^u = \delta\underline{\hat{\mathbf{u}}}^{\mathrm{T}} \underline{\underline{\mathbf{M}}}_e \Delta\underline{\ddot{\hat{\mathbf{u}}}} + \delta\underline{\hat{\mathbf{u}}}^{\mathrm{T}} \underline{\underline{\tilde{\mathbf{K}}}}_e^{uu} \Delta\underline{\hat{\mathbf{u}}}, \tag{33}$$

where

$$\begin{aligned} \underline{\underline{\tilde{\mathbf{K}}}}_e^{uu} =& \underline{\underline{\mathbf{K}}}_e^{uu} + \frac{1}{K_e^{\bar{p}\bar{J}_r}} \underline{\mathbf{K}}_e^{u\bar{J}_r} \underline{\mathbf{K}}_e^{\bar{p}u} + \frac{1}{K_e^{\bar{J}_r\bar{p}}} \underline{\mathbf{K}}_e^{u\bar{p}} \underline{\mathbf{K}}_e^{\bar{J}_r u} \\ &+ \frac{K_e^{\bar{J}_r\bar{J}_r}}{K_e^{\bar{p}\bar{J}_r} K_e^{\bar{J}_r\bar{p}}} \underline{\mathbf{K}}_e^{u\bar{p}} \underline{\mathbf{K}}_e^{\bar{p}u}, \end{aligned} \tag{34}$$

and

$$\begin{aligned} \underline{\underline{\mathbf{K}}}_e^{uu} &= \int_{\Omega_e} \underline{\underline{\mathbf{B}}}_u^{\mathrm{T}} \underline{\underline{\tilde{\mathbf{a}}}}_{uu} \underline{\underline{\mathbf{B}}}_u\, d\Omega_e, \quad \underline{\mathbf{K}}_e^{u\bar{J}_r} = \int_{\Omega_e} \underline{\underline{\mathbf{B}}}_u^{\mathrm{T}} \underline{\tilde{\mathbf{a}}}_{u\bar{J}_r}\, d\Omega_e, \\ \underline{\mathbf{K}}_e^{u\bar{p}} &= \int_{\Omega_e} \underline{\underline{\mathbf{B}}}_u^{\mathrm{T}} \underline{\mathbf{I}}\, d\Omega_e, \quad \underline{\mathbf{K}}_e^{\bar{p}u} = \int_{\Omega_e} \underline{\mathbf{I}}^{\mathrm{T}} \underline{\underline{\mathbf{B}}}_u\, d\Omega_e \\ \underline{\mathbf{K}}_e^{\bar{J}_r u} &= \int_{\Omega_e} \underline{\tilde{\mathbf{a}}}_{\bar{J}_r u} \underline{\underline{\mathbf{B}}}_u\, d\Omega_e, \quad K_e^{\bar{J}_r\bar{J}_r} = \int_{\Omega_e} \tilde{a}_{\bar{J}_r\bar{J}_r}\, d\Omega_e, \\ K_e^{\bar{J}_r\bar{p}} &= K_e^{\bar{p}\bar{J}_r} = \int_{\Omega_e} \frac{\bar{J}_r}{J_r} d\Omega_e. \end{aligned} \tag{35}$$

The mass matrix is expressed by

$$\underline{\underline{\mathbf{M}}}_e = \int_{\Omega_e} \rho_0 \gamma \underline{\underline{\mathbf{N}}}_u^{\mathrm{T}} \underline{\underline{\mathbf{N}}}_u\, d\Omega_e, \tag{36}$$

which is a function of the relative mass density γ. So, the mass can decrease in the fractured region.

3.2. Discretization of the mass balance law

The weak form of the mass balance law is given by $\delta\Pi^\gamma = \sum_{e=1}^{N_{el}} \delta\Pi_e^\gamma = 0$. On the level of a finite element we have

$$\delta\Pi_e^\gamma = \int_{\Omega_e} \left(-\tilde{\mathbf{f}} \cdot \mathrm{grad}\,(\delta\gamma) + \tilde{\zeta}\delta\gamma\right) d\Omega_e, \tag{37}$$

where $\tilde{\mathbf{f}}$ and $\tilde{\zeta}$ are the modified normalized mass flux vector and the modified normalized mass sink scalar, respectively. They are calculated using the modified left Cauchy–Green deformation tensor.

Relative density and virtual relative density are approximated as follows

$$\gamma = \sum_{I=1}^{n_{en}} N_I \hat{\gamma}^I = \underline{\mathbf{N}}_\gamma \underline{\hat{\gamma}}, \quad \delta\gamma = \sum_{I=1}^{n_{en}} N_I \delta\hat{\gamma}^I = \underline{\mathbf{N}}_\gamma \delta\underline{\hat{\gamma}}. \tag{38}$$

For the brick element, for example, $\underline{\hat{\gamma}}$ and $\delta\underline{\hat{\gamma}}$ contain all nodal relative mass densities and all nodal virtual relative mass densities as follows

$$\underline{\hat{\gamma}} = \left\{\hat{\gamma}^1, \hat{\gamma}^2, \ldots, \hat{\gamma}^8\right\}^{\mathrm{T}}, \quad \delta\underline{\hat{\gamma}} = \left\{\delta\hat{\gamma}^1, \delta\hat{\gamma}^2, \ldots, \delta\hat{\gamma}^8\right\}^{\mathrm{T}}. \tag{39}$$

and $\underline{\mathbf{N}}_\gamma$ is a row vector incorporates shape functions as defined in Abu-Qbeitah et al. (2023a). Further, the gradient of virtual relative density takes form

$$\mathrm{grad}\,(\delta\gamma) = \underline{\underline{\mathbf{B}}}_\gamma \delta\underline{\hat{\gamma}}, \tag{40}$$

where $\mathrm{grad}\,(\delta\gamma) = \left\{\mathrm{grad}\,(\delta\gamma)_1, \mathrm{grad}\,(\delta\gamma)_2, \mathrm{grad}\,(\delta\gamma)_3\right\}^{\mathrm{T}}$, and $\underline{\underline{\mathbf{B}}}_\gamma$ is a 3×8 matrix including the derivatives of the nodes' shape functions with respect to the current coordinates.

The mass balance equation is solved using the Newton procedure with the following internal force at the element-level

$$\underline{\hat{\mathbf{F}}}_e^{\gamma,\mathrm{int}} = \int_{\Omega_e} \left(-\underline{\underline{\mathbf{B}}}_\gamma^{\mathrm{T}} \tilde{\mathbf{f}} + \underline{\mathbf{N}}_\gamma^{\mathrm{T}} \tilde{\zeta}\right) d\Omega_e. \tag{41}$$

The linearized form of (37) reads

$$\Delta\delta\Pi_e^\gamma = \delta\underline{\hat{\gamma}}^{\mathrm{T}} \underline{\underline{\mathbf{K}}}_e^{\gamma\gamma} \Delta\underline{\hat{\gamma}}, \tag{42}$$

where

$$\underline{\underline{\mathbf{K}}}_e^{\gamma\gamma} = \int_{\Omega_e} \left(-\underline{\underline{\mathbf{B}}}_\gamma^{\mathrm{T}} \underline{\underline{\tilde{\mathbf{C}}}}_{\gamma\gamma} \underline{\underline{\mathbf{B}}}_\gamma + \underline{\mathbf{N}}_\gamma^{\mathrm{T}} \tilde{C}_{\gamma\gamma} \underline{\mathbf{N}}_\gamma\right) d\Omega_e, \tag{43}$$

and

$$\begin{aligned} \tilde{C}_{\gamma\gamma} &= \frac{\partial\tilde{\mathbf{f}}}{\partial\,(\mathrm{grad}\,(\gamma))} = I^2\tilde{\mathbf{b}}, \\ \tilde{C}_{\gamma\gamma} &= \frac{\partial\tilde{\zeta}}{\partial\gamma}\bigg|_{\left\{J=\bar{J}, \mathbf{b}=\tilde{\mathbf{b}}\right\}} = -\frac{\tilde{I}_3^{1/2}}{\tilde{\mathcal{H}} + \varepsilon}. \end{aligned} \tag{44}$$

3.3. Time integration

The Hilber–Hughes–Taylor (HHT) method (Hilber et al., 1977) is adopted in the present work. It is an implicit time integration technique offered by Abaqus (Smith, 2020), which maintains second order accuracy. For more details about implementing the HHT method, interested readers are referred to Abu-Qbeitah et al. (2023a).

4. Numerical examples

The numerical formulation was implemented using the commercial finite element software Abaqus 2020 (Smith, 2020). The soft matrix and hard inclusions are treated as viscoelastic and elastic materials, respectively.

Specifically, we chose the collagenous material of the abdominal aortic aneurysm (AAA) for the soft matrix and VeroWhite (VW) material for hard inclusions. For such materials, the experimental data exists and the fitted model parameters are presented in Table 1 (Faye et al., 2019; Raghavan and Vorp, 2000; Vero, 2018; Russ et al., 2020).

Below, we present results of the simulations of loading soft composites with various designs. The subtleties of the computational implementation in Abaqus are discussed in detail in Abu-Qbeitah et al. (2023a) and we skip them.

All samples under consideration are three-dimensional with 0.2 mm thickness. Tension is uniaxial in the horizontal direction. Velocity of

Table 1
Matrix and inclusion materials' parameters.

	Φ_A [MPa]	m	k^A_{bulk} [MPa]	k^B_{bulk} [MPa]	c^A_1 [MPa]	c^B_1 [MPa]	c^A_2 [MPa]	c^B_2 [MPa]	l [mm]	ϱ_0 [kg/m^3]	β_2 [MPa s]
Matrix	0.1686	10	500	500	0.617	0.617	1.215	1.215	0.1	1433	0.05
Inclusion	16.86	10	4167	N/A	446	N/A	0.0	N/A	0.1	1180	N/A

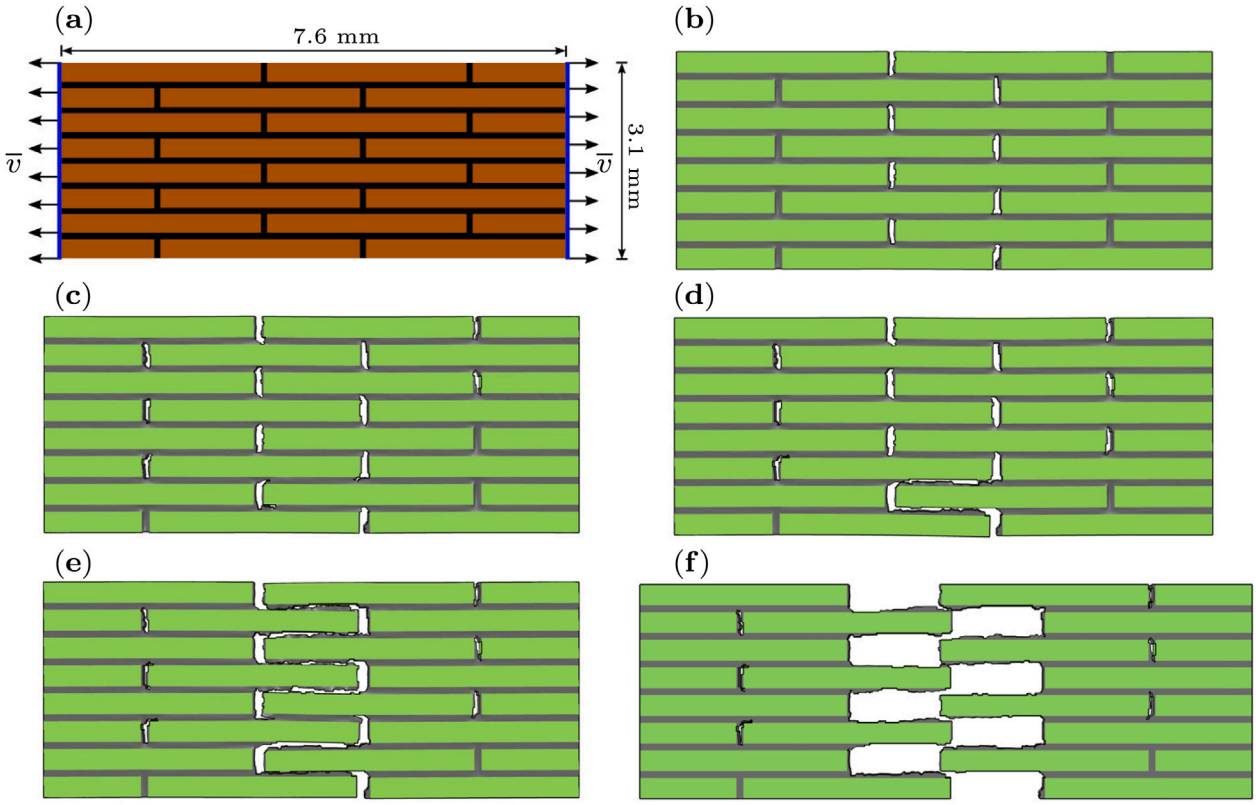

Fig. 2. Offset design: (a) geometry and boundary conditions; (b)–(f) crack evolution under tension.

1 mm/s is applied at the left and right edges of samples. These edges do not move in other directions. The width of the matrix material is 0.1 mm and it is discretized by at least four elements. So, the maximum element size is 0.025 mm, which is one fourth of the characteristic length l. We chose l = 0.1 mm based on its estimate for rubber-like materials given in Volokh (2011) and observations of arterial fracture discussed in Holzapfel and Ogden (2018). We refer the reader to Abu-Qbeitah et al. (2023b), for example, for a discussion of the mesh sensitivity issues.

4.1. Offset design

In the first example of the composite design, the inclusions are arranged in an offset manner, which are bonded by the softer material of the matrix as shown in Fig. 2(a). This staggered design is commonly found in nature, e.g., nacre, seashells, bone, teeth etc. Slesarenko et al. (2017b).

The offset sample is discretized by 39,465 unstructured eight-node brick elements with one element throughout the sample's thickness.

Fig. 2 shows fracture onset and propagation in the described sample under uniaxial tension. First, cracks initiate and propagate along short edges of inclusions. Then, the vertical cracks connect horizontally along long edges of inclusions until the total breakage of the sample. Such scenario is clearly observed in physical experiments — see Slesarenko et al. (2017b).

Fig. 3 shows the average – for the whole sample – stress–stretch curve at the subsequent stages of fracture. It can be noted that the average stress can drop and increases again when new local cracks appear and propagate. The reason is that at the beginning of damage, cracks propagate at short edges of inclusions, leading to a decrease in the load bearing capacity. However, these cracks release the stress concentrators what, in its turn, strengthens the remaining structure.

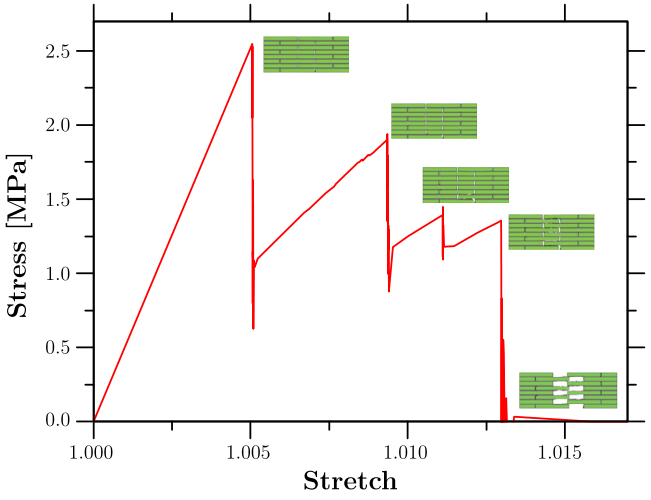

Fig. 3. Average stress–stretch curve for the offset design under uniaxial tension. Limit points correspond to the fracture patterns shown in Fig. 2.

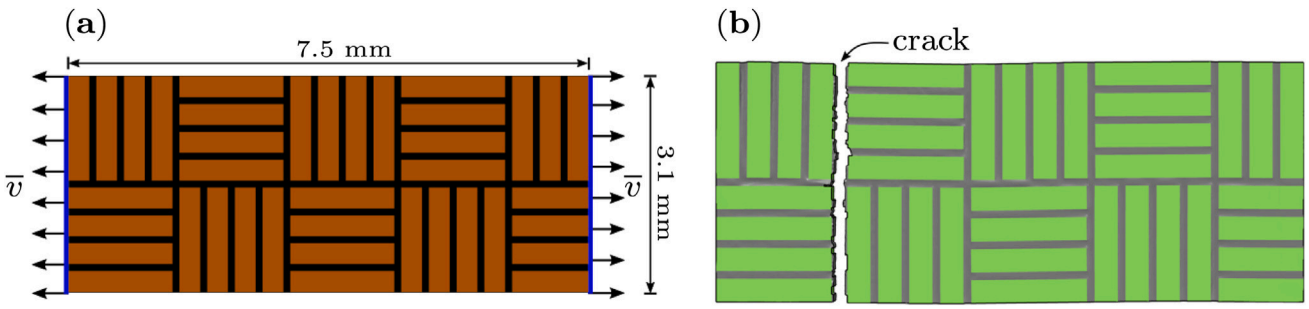

Fig. 4. Crosshatch design: (a) geometry and boundary conditions; (b) deformed shape depicting crack evolution.

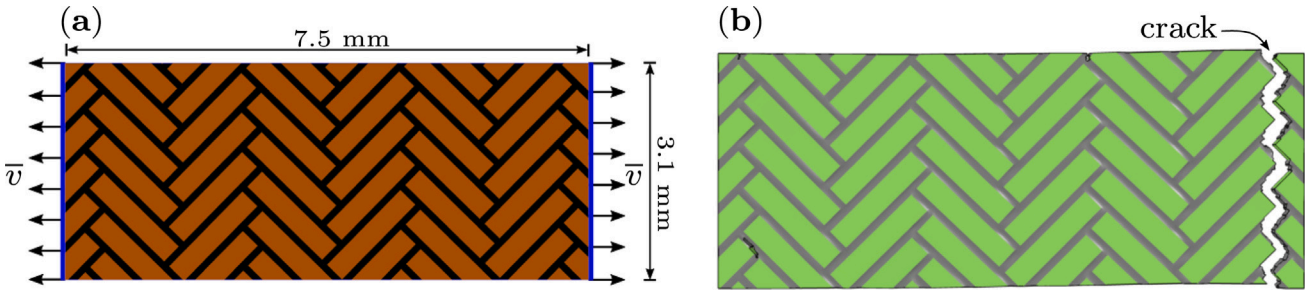

Fig. 5. Herringbone design: (a) geometry and boundary conditions; (b) deformed shape depicting crack evolution.

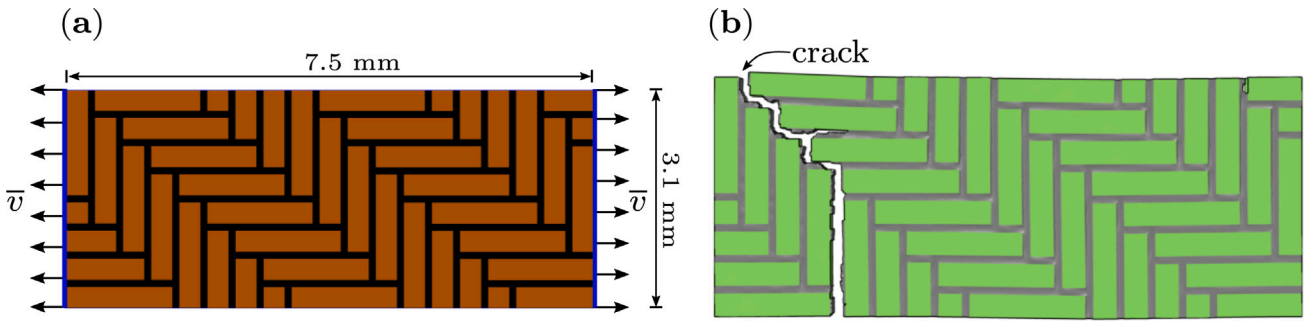

Fig. 6. Straight herringbone design: (a) geometry and boundary conditions; (b) deformed shape depicting crack evolution.

It should be noticed that to destroy the sample completely, cracks need to propagate both vertically and horizontally, passing long distances, which makes this composite tough to fracture.

We also emphasize that the appearance of specific cracks depends on the specific unstructured finite-element mesh. Unstructured meshes induce inhomogeneity in calculations similar to the behavior of real materials, which are not ideally homogeneous.

4.2. Crosshatch design

The inclusions in this design are arranged as shown in Fig. 4(a). The domain is discretized by 38,798 unstructured eight-node brick elements with one element throughout the sample thickness.

Fig. 4(b) shows final stage of fracture. The crack initiates in the matrix inside the sample at the corner of the inclusion. Then, the crack propagates vertically cutting the sample into two pieces.

Fig. 7 shows the average stress–stretch curve for this design. It can be noticed that once the crack initiates and propagates there is no increase in the load bearing capacity of the sample. Nothing stops the crack propagation. The fracture is one-step catastrophic.

It can also be noticed that the crosshatch design shows relatively high stiffness comparable with the one of the offset design.

4.3. Herringbone design

The herringbone design is achieved by arranging the inclusions as shown in Fig. 5(a). The inclusions in this design are inclined at the angle of 45°. The sample is discretized by using 81,116 unstructured eight-node brick elements with two elements throughout the sample thickness.

Fig. 5(b) shows the final stage of fracture. The specimen cracks in a path perpendicular to the loading direction following the twining of the matrix. Fig. 7 shows the average stress–stretch curve with the one-step catastrophic fracture.

The straight herringbone design is depicted in Fig. 6(a). The sample is discretized by 38,968 unstructured eight-node brick elements with one element throughout the sample thickness.

The destroyed sample is shown in Fig. 6(b). It is clear that the fracture involves one catastrophic fracture step that appears on the stress–stretch curve as shown in Fig. 7. The strength of this design was higher than the one of the previous herringbone design.

It can be noticed from Fig. 7 that the stress and stretch at which material fractures is almost the same for both the crosshatch and the straight herringbone designs. It can also be seen from Fig. 7 that the offset design is the only one that has multiple fracture steps. Further, the strength of the offset sample is more than five times the strength of the homogeneous sample (i.e., matrix only).

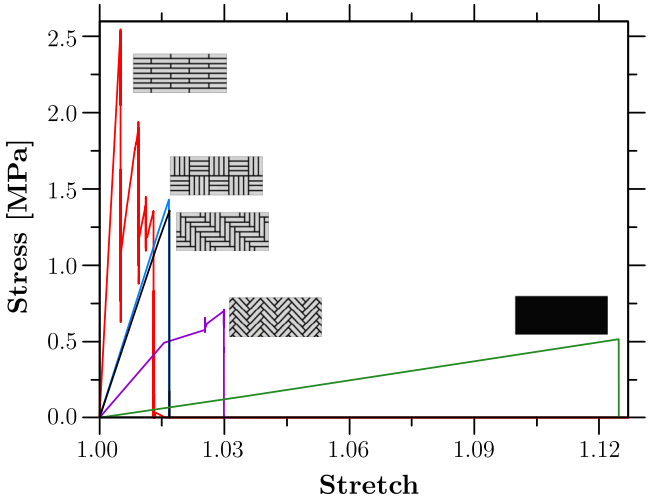

Fig. 7. Average stress–stretch curves for all designs under uniaxial tension. The black rectangle represents the purely homogeneous matrix without inclusions.

4.4. Inclined offset design

Finally, the staggered offset design shown in Fig. 2(a) is modified by varying the angles of inclination of inclusions: $\alpha = 0°$, $30°$, and $90°$, respectively. The samples still undergo uniaxial tension in the horizontal direction as shown in Fig. 2(a).

Fig. 8 shows the final fracture pattern in each case. Fig. 9 shows the average stress–stretch curves for each case. The best crack resistance is achieved when $\alpha = 0°$, where the crack path is the longest one. The latter observation favors the nature choice of material design.

4.5. Dissipated energies

The dissipated energy for each damaged element as a result of crack propagation is determined using the failure energy as follows (Volokh, 2019; Abu-Qbeitah et al., 2023b)

$$U_i = v_i \psi_{\mathrm{f}} = v_i \Phi m^{-1} \Gamma[m^{-1}, W(\mathbf{I})^m \Phi^{-m}], \tag{45}$$

where v_i is the referential volume of the ith damaged element, and ψ_{f} designates the constant bulk failure energy.

Substituting for the energy limiter Φ and the sharpness parameter m in (45) and evaluating the upper incomplete gamma function yields

$$U_i = 0.95 v_i \Phi. \tag{46}$$

Fig. 10 shows the dissipated energy values for all samples analyzed in this study. It can be noticed that the maximum energy is dissipated for the staggered offset design! It has the highest first rank. Other cases are properly ranked in the descendent order in accordance with the amount of the dissipated energy.

5. Conclusions

We computationally simulated uniaxial tension of soft composites with various designs: offset, inclined offset, crosshatch, herringbone and straight herringbone.

For the simulations, we used the "first principles" of continuum mechanics without involving simplifying geometrical assumptions. We combined the material-sink theory coupling momenta and mass balance equations with the visco-hyper-elastic constitutive model at finite strains.

We implemented this nonlinear continuum mechanics theory within the Abaqus finite element software and performed various numerical simulations. These simulations provided fracture patterns as well as the maximum achievable stress – strength – and dissipated energy – toughness – for the considered samples.

We emphasize that the presented results were obtained for the case of uniaxial loading — 'in-silico' tension experiments. They suggest that among the examined the nature-made staggered offset design is the best one because it provides the highest strength and toughness — the dissipated fracture energy. Evidently, our results and conclusions are limited by the considered loading. It would be interesting to simulate behavior of the staggered soft composites under different loading scenarios.

CRediT authorship contribution statement

Suhib Abu-Qbeitah: Writing – original draft, Visualization, Validation, Software, Investigation. **Mahmood Jabareen:** Writing – review & editing, Validation, Supervision, Software, Methodology, Conceptualization. **Konstantin Y. Volokh:** Writing – review & editing, Supervision, Methodology, Funding acquisition, Conceptualization.

Declaration of competing interest

The authors declare that they have no known competing financial interests or personal relationships that could have appeared to influence the work reported in this paper.

Data availability

Data will be made available on request.

Acknowledgments

The support from the Israel Science Foundation (ISF-394/20) as well as the Israeli Ministry of Science and Technology (MOST-0005173) is gratefully acknowledged. Also, M. Jabareen is supported by Neubauer Foundation.

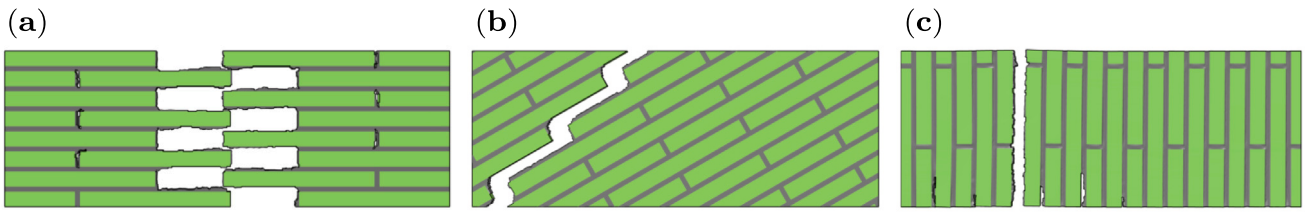

Fig. 8. Fractured samples for various offset designs with different inclination angles: (a) $\alpha = 0°$, (b) $\alpha = 30°$, and (c) $\alpha = 90°$.

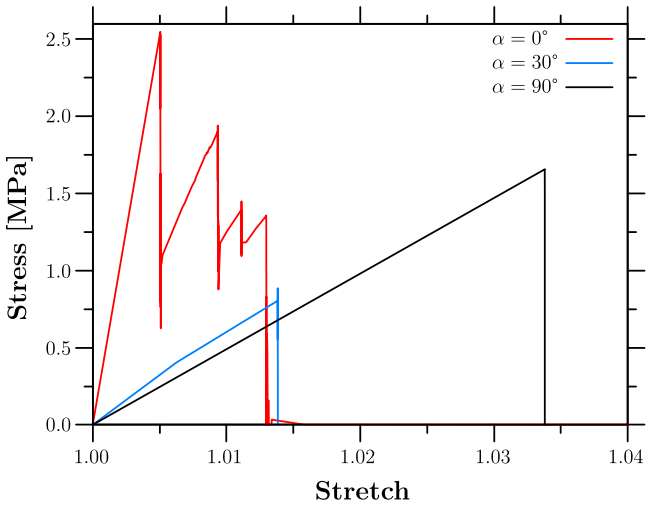

Fig. 9. Average stress–stretch curves for the offset designs with different inclination angles under uniaxial tension.

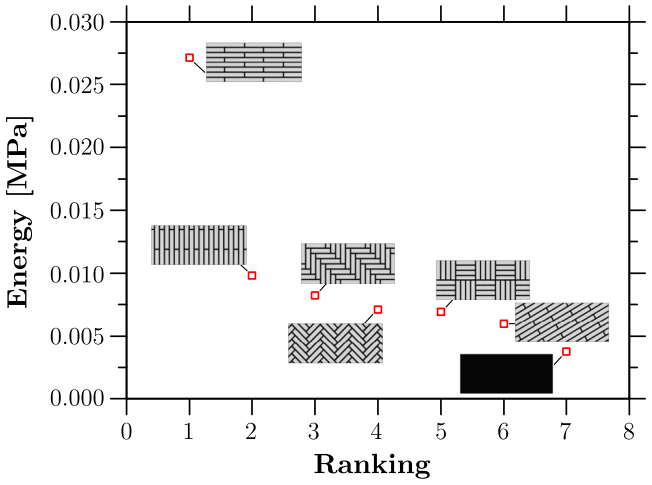

Fig. 10. Dissipated energies for the all modeled arrangements. The black rectangle represents the homogeneous case where the matrix material does not have inclusions.

References

Abu-Qbeitah, S., Jabareen, M., Volokh, K.Y., 2022. Dynamic versus quasi-static analysis of crack propagation in soft materials. J. Appl. Mech. 89 (12), 121008.

Abu-Qbeitah, S., Jabareen, M., Volokh, K.Y., 2023a. Modeling cracks in viscoelastic materials at finite strains. Internat. J. Numer. Methods Engrg. e7398.

Abu-Qbeitah, S., Jabareen, M., Volokh, K.Y., 2023b. Quasi-static crack propagation in soft materials using the material-sink theory. Int. J. Mech. Sci. 248, 108160.

Bai, H., Walsh, F., Gludovatz, B., Delattre, B., Huang, C., Chen, Y., Tomsia, A.P., Ritchie, R.O., 2016. Bioinspired hydroxyapatite/poly(methyl methacrylate) composite with a Nacre-Mimetic architecture by a bidirectional freezing method. Adv. Mater. 28 (1), 50–56.

Barber, A.H., Lu, D., Pugno, N.M., 2015. Extreme strength observed in limpet teeth. J. R. Soc. Interface 12 (105), 20141326.

Barthelat, F., Espinosa, H.D., 2007. An experimental investigation of deformation and fracture of Nacre–Mother of pearl. Exp. Mech. 47 (3), 311–324.

Barthelat, F., Li, C.-M., Comi, C., Espinosa, H.D., 2006. Mechanical properties of Nacre constituents and their impact on mechanical performance. J. Mater. Res. 21 (8), 1977–1986.

Barthelat, F., Rabiei, R., 2011. Toughness amplification in natural composites. J. Mech. Phys. Solids 59 (4), 829–840.

Barthelat, F., Rim, J., Espinosa, H., 2009. A review on the structure and mechanical properties of mollusk shells – perspectives on synthetic biomimetic materials. In: Applied Scanning Probe Methods XIII: Biomimetics and Industrial Applications. Springer Berlin Heidelberg, Berlin, Heidelberg, pp. 17–44.

Barthelat, F., Tang, H., Zavattieri, P., Li, C.-M., Espinosa, H., 2007. On the mechanics of mother-of-pearl: A key feature in the material hierarchical structure. J. Mech. Phys. Solids 55 (2), 306–337.

Bhushan, B., 2009. Biomimetics: lessons from nature–an overview. Phil. Trans. R. Soc. A 367 (1893), 1445–1486.

Bonderer, L.J., Studart, A.R., Gauckler, L.J., 2008. Bioinspired design and assembly of platelet reinforced polymer films. Science 319 (5866), 1069–1073.

Cho, H., Weaver, J.C., Pöselt, E., in't Veld, P.J., Boyce, M.C., Rutledge, G.C., 2016. Engineering the mechanics of heterogeneous soft crystals. Adv. Funct. Mater. 26 (38), 6938–6949.

Currey, J.D., 1999. The design of mineralised hard tissues for their mechanical functions. J. Exp. Biol. 202 (23), 3285–3294.

Currey, J.D., Sheppard, P.M., 1977. Mechanical properties of mother of pearl in tension. Proc. R. Soc. B 196 (1125), 443–463.

Dalaq, A.S., Abueidda, D.W., Abu Al-Rub, R.K., 2016. Mechanical properties of 3D printed interpenetrating phase composites with novel architectured 3D solid-sheet reinforcements. Composites A 84, 266–280.

Dimas, L.S., Bratzel, G.H., Eylon, I., Buehler, M.J., 2013. Tough composites inspired by mineralized natural materials: Computation, 3D printing, and testing. Adv. Funct. Mater. 23 (36), 4629–4638.

Faye, A., Lev, Y., Volokh, K.Y., 2019. The effect of local inertia around the crack-tip in dynamic fracture of soft materials. Mech. Soft Mater. 1 (1), 4.

Gu, G.X., Libonati, F., Wettermark, S.D., Buehler, M.J., 2017. Printing nature: Unraveling the role of Nacre's mineral bridges. J. Mech. Behav. Biomed. Mater. 76, 135–144.

Hilber, H., Hughes, T., Taylor, R., 1977. Improved numerical dissipation for time integration algorithms in structural dynamics. Earthq. Eng. Struct. Dyn. 5 (3), 283–292.

Holzapfel, G.A., Ogden, R.W., 2018. Multiscale Soft Tissue Mechanics and Mechanobiology. Springer.

Huang, Z., Li, H., Pan, Z., Wei, Q., Chao, Y.J., Li, X., 2011. Uncovering high-strain rate protection mechanism in Nacre. Sci. Rep. 1 (1), 148.

Kakisawa, H., Sumitomo, T., 2011. The toughening mechanism of Nacre and structural materials inspired by Nacre. Sci. Technol. Adv. Mater. 12, 064710.

Khayer Dastjerdi, A., Barthelat, F., 2015. Teleost fish scales amongst the toughest collagenous materials. J. Mech. Behav. Biomed. Mater. 52, 95–107, SI:Collagen mechanics.

Li, Y., He, H., Wang, Q., Zhang, L., Yu, Y., He, D., 2022. Bioinspired diamond composites and their dynamic shock performance. Mech. Mater. 164, 104105.

Libonati, F., 2016. Bio-inspired composites: Using nature to tackle composite limitations. In: Advanced Engineering Materials and Modeling. John Wiley and Sons, pp. 165–190.

Libonati, F., Colombo, C., Vergani, L., 2014. Design and characterization of a biomimetic composite inspired to human bone. Fatigue Fract. Eng. Mater. Struct. 37 (7), 772–781.

Libonati, F., Vergani, L., 2016. Understanding the structure–property relationship in cortical bone to design a biomimetic composite. Compos. Struct. 139, 188–198.

Luz, G.M., Mano, J.F., 2010. Mineralized structures in nature: Examples and inspirations for the design of new composite materials and biomaterials. Compos. Sci. Technol. 70 (13), 1777–1788, ICCM-17: Composites In Biomedical Applications.

Magrini, T., Bouville, F., Lauria, A., Le Ferrand, H., Niebel, T.P., Studart, A.R., 2019. Transparent and tough bulk composites inspired by Nacre. Nature Commun. 10 (1), 2794.

Menig, R., Meyers, M., Meyers, M., Vecchio, K., 2000. Quasi-static and dynamic mechanical response of haliotis rufescens (abalone) shells. Acta Mater. 48 (9), 2383–2398.

Milwich, M., Speck, T., Speck, O., Stegmaier, T., Planck, H., 2006. Biomimetics and technical textiles: solving engineering problems with the help of nature's wisdom. Am. J. Bot. 93 (10), 1455–1465.

Peng, J., Huang, C., Cao, C., Saiz, E., Du, Y., Dou, S., Tomsia, A.P., Wagner, H.D., Jiang, L., Cheng, Q., 2020. Inverse Nacre-like epoxy-graphene layered nanocomposites with integration of high toughness and self-monitoring. Matter 2 (1), 220–232.

Rabiei, R., Bekah, S., Barthelat, F., 2010. Failure mode transition in Nacre and bone-like materials. Acta Biomater. 6 (10), 4081–4089.

Raghavan, M.L., Vorp, D.A., 2000. Toward a biomechanical tool to evaluate rupture potential of abdominal aortic aneurysm: identification of a finite strain constitutive model and evaluation of its applicability. J. Biomech. 33 (4), 475–482.

Ritchie, R.O., 2011. The conflicts between strength and toughness. Nature Mater. 10 (11), 817–822.

Rudykh, S., Boyce, M.C., 2014. Transforming wave propagation in layered media via instability-induced interfacial wrinkling. Phys. Rev. Lett. 112, 034301.

Russ, J., Slesarenko, V., Rudykh, S., Waisman, H., 2020. Rupture of 3D-printed hyperelastic composites: Experiments and phase field fracture modeling. J. Mech. Phys. Solids 140, 103941.

Slesarenko, V., Kazarinov, N., Rudykh, S., 2017a. Distinct failure modes in bio-inspired 3D-printed staggered composites under non-aligned loadings. Smart Mater. Struct. 26 (3).

Slesarenko, V., Volokh, K.Y., Aboudi, J., Rudykh, S., 2017b. Understanding the strength of bioinspired soft composites. Int. J. Mech. Sci. 131–132, 171–178.

Smith, M., 2020. ABAQUS/Standard Documentation, Version 2020. Dassault Systèmes Simulia Corp, Johnston, RI, USA.
Studart, A.R., 2012. Towards high-performance bioinspired composites. Adv. Mater. 24 (37), 5024–5044.
Tang, Z., Kotov, N.A., Magonov, S., Ozturk, B., 2003. Nanostructured artificial Nacre. Nature Mater. 2 (6), 413–418.
Vero, 2018. Material data sheet.
Volokh, K.Y., 2007. Hyperelasticity with softening for modeling materials failure. J. Mech. Phys. Solids 55 (10), 2237–2264.
Volokh, K.Y., 2010. On modeling failure of rubber-like materials. Mech. Res. Commun. 37 (8), 684–689.
Volokh, K.Y., 2011. Characteristic length of damage localization in rubber. Int. J. Fract. 168, 113–116.
Volokh, K.Y., 2013. Review of the energy limiters approach to modeling failure of rubber. Rubber Chem. Technol. 86 (3), 470–487.
Volokh, K., 2014. On irreversibility and dissipation in hyperelasticity with softening. J. Appl. Mech. Trans. ASME 81 (7).
Volokh, K.Y., 2017. Fracture as a material sink. Mater. Theory 1 (1), 3.
Volokh, K.Y., 2019. Mechanics of Soft Materials, second ed. Springer, Singapore.
Wegst, U.G.K., Ashby, M.F., 2004. The mechanical efficiency of natural materials. Phil. Mag. 84 (21), 2167–2186.
Wegst, U.G.K., Bai, H., Saiz, E., Tomsia, A.P., Ritchie, R.O., 2015. Bioinspired structural materials. Nature Mater. 14 (1), 23–36.
Weickenmeier, J., Jabareen, M., 2014. Elastic-viscoplastic modeling of soft biological tissues using a mixed finite element formulation based on the relative deformation gradient. Int. J. Numer. Methods Biomed. Eng. 30 (11), 1238–1262.
Zhao, H., Yue, Y., Guo, L., Wu, J., Zhang, Y., Li, X., Mao, S., Han, X., 2016. Cloning Nacre's 3D interlocking skeleton in engineering composites to achieve exceptional mechanical properties. Adv. Mater. 28 (25), 5099–5105.